



Image-Based Computational Fluid Dynamics to Compare Two Repair Techniques for Mitral Valve Prolapse

Lorenzo Bennati¹ · Giovanni Puppini² · Vincenzo Giamb Bruno³ · Giovanni Battista Luciani³ · Christian Vergara⁴

Received: 29 December 2023 / Accepted: 29 July 2024
© The Author(s) 2024

Abstract

Objective The treatment of mitral valve prolapse involves two distinct repair techniques: chordal replacement (Neochordae technique) and leaflet resection (Resection technique). However, there is still a debate in the literature about which is the optimal one. In this context, we performed an image-based computational fluid dynamic study to evaluate blood dynamics in the two surgical techniques.

Methods We considered a healthy subject (H) and two patients (N and R) who underwent surgery for prolapse of the posterior leaflet and were operated with the Neochordae and Resection technique, respectively. Computational Fluid Dynamics (CFD) was employed with prescribed motion of the entire left heart coming from cine-MRI images, with a Large Eddy Simulation model to describe the transition to turbulence and a resistive method for managing valve dynamics. We created three different virtual scenarios where the operated mitral valves were inserted in the same left heart geometry of the healthy subject to study the differences attributed only to the two techniques.

Results We compared the three scenarios by quantitatively analyzing ventricular velocity patterns and pressures, transition to turbulence, and the ventricle ability to prevent thrombi formation. From these results, we found that the operative techniques affected the ventricular blood dynamics in different ways, with variations attributed to the reduced mobility of the Resection posterior leaflet. Specifically, the Resection technique resulted in turbulent forces, related with the risk of hemolysis formation, up to 640 Pa, while the other two scenarios exhibited a maximum of 240 Pa. Moreover, in correspondence of the ventricular apex, the Resection technique reduced the areas with low velocity to 15%, whereas the healthy case and the Neochordae case maintained these areas at 30 and 48%, respectively. Our findings suggest that the Neochordae technique developed a more physiological flow with respect to the Resection technique.

Conclusion Resection technique gives rise to a different direction of the mitral jet during diastole increasing the ability to washout the ventricular apex preventing from thrombi formation, but at the same time it promotes turbulence formation that is associated with ventricular effort and risk of hemolysis.

Keywords Mitral valve prolapse · Neochordae technique · Resection technique · Computational fluid dynamics · Turbulence · Hemolysis

Introduction

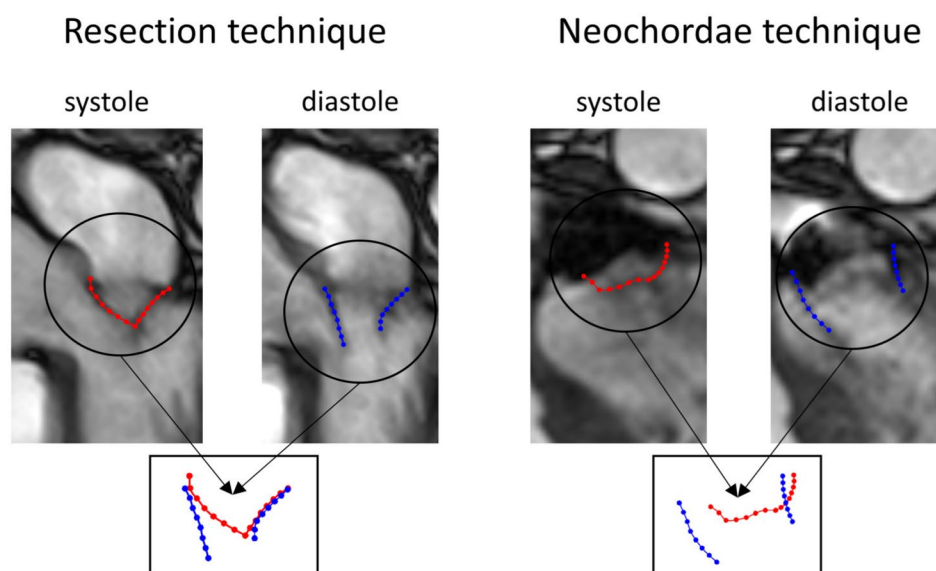
Mitral Valve Prolapse (MVP) is a valvular disease characterized by an unphysiological displacement of the leaflets toward the left atrium during the systolic phase due to elongated or broken chordae tendineae. The main consequence is mitral regurgitation.

Nowadays, there are two different surgical repair philosophies to treat MVP: the *Resection* technique and the *Neochordae* technique. In the first one, the surgeon excises the prolapsed portion of the leaflet (and associated ruptured or elongated chordae) and reconstructs the leaflet by direct suture, restoring the coaptation surface [1–3]. This technique has been established as the gold standard for the treatment of posterior leaflet MVP [2, 3]. However, the main disadvantage is related to the fact that the higher the portion of tissue removed, the lower the leaflet mobility, practically resulting in a mono-cuspid mitral valve, see Fig. 1, left [4].

Associate Editor Joel Stitzel oversaw review of this article.

Extended author information available on the last page of the article

Fig. 1 Left: Cine-MRI images of a patient operated with Resection technique to treat the posterior leaflet prolapse of the P2 segment. We reported the leaflets contours in closed (red) and open (blue) configurations. Notice that the posterior (operated) leaflet has a reduced mobility as a consequence of the reparative technique. Right: Cine-MRI images of a patient operated with the Neochordae technique. Notice that this technique ensures greater mobility of the posterior leaflet



To overcome the hypo-mobility of the operated leaflet, Neochordae technique has been introduced [5, 6]. This method is also called *Respect* approach as repair involves placement of artificial chordae and a minimal to no leaflet resection. In particular, a set of pre-made polytetrafluoroethylene (ePTFE) chordae are anchored to the papillary muscles and then used to resuspend the prolapsed segment of the leaflet, see Fig. 1, right. The main drawback of this technique is the need to define the appropriate length for neochordae [7] that often requires a trial-and-error approach during the surgical procedure. Although the long-term results are promising [8], there is still debate in the clinical world about which techniques to use and the relative effects on ventricular fluid dynamics [3]. In this respect, computational methods represent a valuable and non-invasive tool to quantitatively assess the 3D local velocity patterns in the heart chambers and areas of disturbed flow to enhance the understanding of cardiac pathophysiology [9–14] and the design of valve prosthesis or surgical interventions [13, 15–19]. In particular, prior in silico works addressed the issue of studying the two surgical techniques mentioned above. This can be grouped in two categories: *Structure-only* (S), where no blood dynamics is simulated, and *Fluid–Structure Interaction* (FSI) models. Regarding the first approach, we cite [20] where the authors developed a computational simulation protocol to perform virtual Resection technique, whereas other works investigated different neochordae implantation sites [21] and [22, 23] different neochordae tensioning and lengths. To the best of our knowledge, only [24] performed a virtual comparison of the two reparative techniques starting from an ideal mitral valve in presence of posterior leaflet prolapse. For the FSI approach, we cite [13] where the optimal number of neochordae has been investigated in

different types of prolapse obtained by virtually deforming a healthy mitral valve. The results of all these works highlighted that both techniques restored a physiological mitral valve function by reducing the mechanical forces acting on the treated leaflet [20–24]. In particular, Neochordae technique provided better leaflet coaptation and greater posterior leaflet mobility [24], with no marked differences in the hemodynamics with respect to a healthy scenario [13]. On the other hand, Resection technique gave rise to a more uniform stress distribution on the posterior leaflet [24].

In this context, the aim of our work is to compare the two reparative techniques to investigate their effects on the ventricular blood flow. To do this, we used computational fluid dynamics (CFD) with imposed motion where the displacement of the left heart (left ventricle, left atrium, aortic root, mitral, and aortic valve) is provided by dynamic imaging (*Dynamic Image-Based CFD*, DIB-CFD) [25–29]. The choice of using a DIB-CFD model is motivated by the availability of time-resolved cine-MRI images of two repaired mitral valves together with the left heart wall motion. This allows us to focus on and compare hemodynamic quantities, such as velocity, pressure, and turbulence quantities.

Specifically, we reconstructed three different mitral valves (one healthy and two operated with the two techniques) geometries and motion, and we created three different virtual scenarios where the mitral valves are inserted in the same healthy ventricular geometry and motion, supposed to be the same for the three cases. DIB-CFD is then run for the three cases in the same hemodynamic settings. This virtual comparison is employed to emphasize hemodynamic variations due solely to the geometric differences induced by the different techniques independently from changes of

Table 1 Values of the age, BSA, EDV, ESV, EF, and E/A for each patient

Patient	Age [–]	BSA [m ²]	EDV [mL]	ESV [mL]	EF [%]	E/A [–]
H	33	2.14	216	81	62	3.0
N	57	2.04	197	79	60	1.6
R	78	1.87	169	82	51	NA

ventricular geometry and function, which are consequences of long-standing mitral regurgitation.

To the best of our knowledge, the present study features two novelties:

- The reconstruction of the patient-specific mitral valve geometries of two cases, one for each of the repair surgical techniques. Specifically, we also reconstructed the patient-specific motion of such valves;
- A computational comparison of hemodynamics in the two repair technique configurations, including the potential risk of red blood cell damage, ventricular washout, and remodeling indices [30, 31].

To perform this comparison, we used a fluid dynamic incompressible model for blood with a resistive method to treat the presence of the valves and a Large Eddy Simulation (LES) model to account for the transition to turbulence, and we compared different hemodynamic meaningful indices.

Materials and Methods

Creation of the Virtual Scenarios

We considered a healthy subject (H) and two patients (N and R) operated at the Division of Cardiac Surgery, University of Verona, with the Neochordae and the Resection techniques, respectively, due to the prolapse of the P2 segment of the posterior leaflet with no mitral regurgitation. For each of them, post-repair cine-MRI images were available. Ethical review board approval and informed consent were obtained from all subjects. In Table 1, we reported some information about the patients, including the age, Body Surface Area (BSA) [32], End-Diastolic Volume (EDV), End-Systolic Volume (ESV), Ejection Fraction (EF) and the ratio between the peak mitral flow at the E-wave and A-wave (E/A).

We started by the reconstructed motion of the internal wall of the left ventricle, left atrium, and aortic root of case H, obtained from 30 cine-MRI frames as reported in [33]. In Fig. 2A, we display this left heart (LH) displacement $\mathbf{d}_{LH}^i(\mathbf{x})$, $i = 1, \dots, 30$, (with respect to the end-systolic ventricular configuration) at three representative frames, together with the corresponding time evolution of ventricular volume and flow rate through aortic and mitral orifices

computed by means of the cine-MRI images, see Fig. 2B, C. Moreover, we have at disposal also the aortic valve (AV) geometry in the closed and open configurations, see Fig. 2D. From these, we computed the displacement $\mathbf{d}_{AV}(\mathbf{x})$ as the difference between the open and closed states.

For case H, we have also cine-MRI images of the mitral valve consisting in 30 frames per heartbeat acquired following the *ad hoc* protocol proposed in [34] and based on a radial sampling, which are here reconstructed for the first time. Specifically, we reconstructed the geometries and we computed the corresponding displacement $\mathbf{d}_{MV}^i(\mathbf{x})$, $i = 1, \dots, 30$, at all the frames with respect to the end-diastolic configuration, employing the method proposed in [25, 34] (see the Results Section). Briefly, this method is based on the segmentation of the valve leaflets in each plane to obtain a 3D point cloud that is then fitted by means of a B-Spline and turned into a surface mesh of triangles. Furthermore, for each of the two operated cases (N and R), new cine-MRI images of the mitral valve, consisting in 30 acquisitions per heartbeat, were provided. Ethical review board approval and informed consent for the study from both the patients were obtained. The image acquisitions were performed one week after the surgery. Also for these operated cases, we reconstructed the geometries and calculated the corresponding displacement $\mathbf{d}_{MV}^i(\mathbf{x})$ of the mitral valve at all the available frames with respect to the end-diastolic configuration (see the Results Section). Then, the geometries of the two mitral valves were virtually inserted onto the valvular annulus plane of H and adapted to the 30 reconstructions at disposal of the left heart of the healthy subject H, see Fig. 2A. Specifically, in the healthy case H, the mitral annulus were already completely adhered, frame by frame, to the ventricle. Instead, for the operated patients (N and R), we firstly rototranslated, frame by frame, the two mitral valves in order to align their center of mass with that of the healthy mitral valve. Subsequently, we computed the minimum distance of the two operated mitral annuli (N and R) with respect to the healthy annulus. Then, we harmonically extended this distance across all the two operated mitral valves using harmonic extension algorithms. Finally, we warped the two mitral valves based on this displacement. The entire process was performed in the Vascular Modeling ToolKit (VMTK) [35, 36], using the functions *vmtkicpregistration* and *vmtksurfaceharmonicsolver*. The entire process was

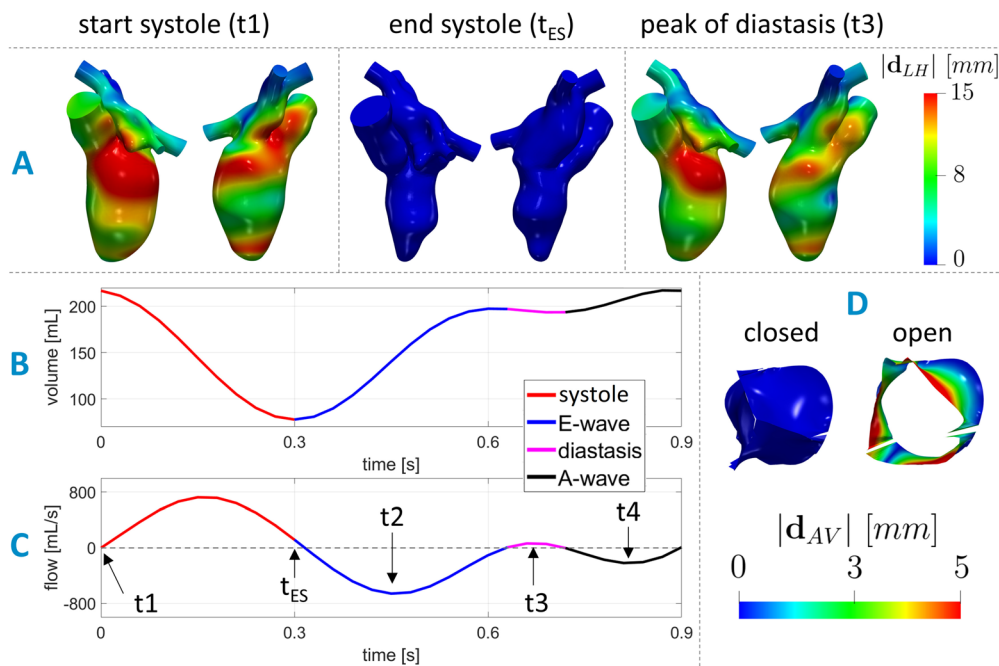


Fig. 2 Geometric and dynamic data taken from [25]. **A** Two views of the geometries and magnitude of the LH displacement $\mathbf{d}_{LH}^i(\mathbf{x})$, $i = 1, \dots, 30$, at the begin of systole t_1 (closed mitral valve), end systole (t_{ES}) (closed mitral valve), the instant t_2 of maximum valve opening (peak of flow rate during E-wave), the instant t_3 of maximum ventricular flow rate during diastasis (i.e., the period of partial closure between the two waves), and the instant t_4 of maximum valve opening during the A-wave (peak of flow rate during

A-wave). **B** Trend in time of the ventricular reconstructed volume. **C** Flow rate through the aortic (from 0 to 0.3 s) and mitral orifice (from 0.3 to 0.9 s). The arrows refer to the end-diastolic frame (t_1), end-systolic frame (t_{ES}), peak of E-wave (t_2), peak of diastasis (t_3), and peak of A-wave (t_4); **D** Geometries and magnitude of the aortic valve displacement $\mathbf{d}_{AV}(\mathbf{x})$ in its fully closed and fully open configuration

done by preserving the same ratio between the area of the annulus and the area of the mitral orifice at the peak of the E-wave measured from imaging for the two patients. In particular, this ratio is equal to 0.52 and 0.63 for N and R, respectively. Notice that, through the inspection of medical images, we found for N and R that the full opening and closure phases required the same number of frames as in the healthy case. Therefore, the three mitral valves (H, N, and R) are synchronized with the myocardial displacement of H during the opening and closure, even if they have different durations of the heartbeat (66 bpm for H, 73 for N, and 85 for R). In this respect, in the numerical experiments we consider the same heartbeat for all three scenarios, equal to that of the healthy scenario (66 bpm).

We remind that the idea of this work is to compare, by means of a computational analysis, the blood dynamics in the two post-operative scenarios N and R with the healthy case, using for all the three scenarios the same ventricular geometry and motion, thus highlighting the differences due to only the reparative technique. Specifically, our choice on using the left ventricle of the healthy case was motivated by the need not to create any bias. In Fig. 3, we displayed the three reconstructed virtual scenarios.

Mathematical and Numerical Modeling

We considered blood as an incompressible, homogeneous, Newtonian fluid with density $\rho = 1.06 \cdot 10^3 \text{ kg/m}^3$ and dynamic viscosity $\mu = 3.5 \cdot 10^{-3} \text{ Pa} \cdot \text{s}$, described by the Navier–Stokes (NS) equations, see [37, 38]. To solve NS in the moving LH, we used the Arbitrary Lagrangian Eulerian (ALE) framework [39] and to manage the presence of the valves we used the Resistive Immersed Implicit Surface (RIIS) method [40, 41]. Specifically, the RIIS method introduces into the momentum balance of the Navier–Stokes equations an additional term, which penalizes the kinematic condition representing the adherence of the blood to the valves. The main advantage of this method is that the fluid and valve computational meshes do not need to be conforming at the interface and that it circumvents any fluid mesh deformation due to the interaction with the valve¹. To evaluate the transition to turbulence occurring in the left

¹ Notice that the underlying fluid mesh deforms by means of the ALE approach according to the prescribed myocardial movement. Here, we are stating that there is no relative deformation with respect to the valve movement.

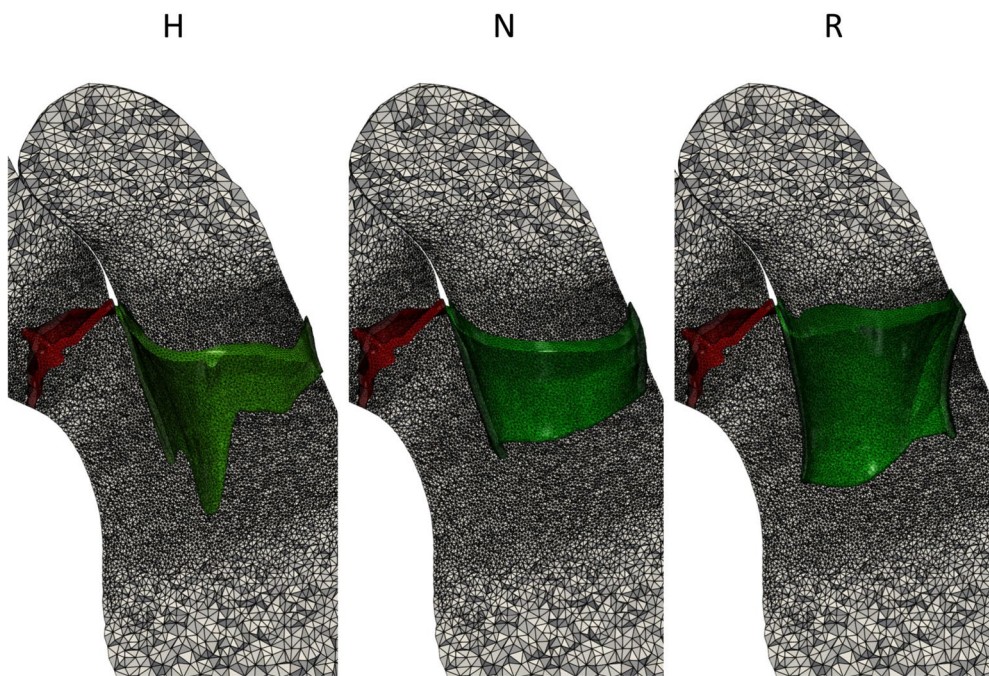
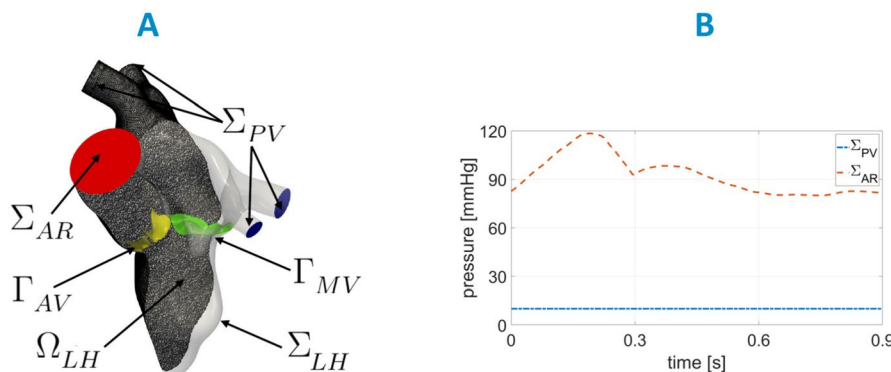


Fig. 3 Computational mesh of three virtual scenarios: Healthy (H), Neochordae (N), and Resection (R). In red, we displayed the aortic valve and in green, the mitral valve

Fig. 4 **A** Computational domain Ω with its boundaries. In yellow, we reported the aortic valve Γ_{AV} and in green, the mitral valve Γ_{MV} of H. **B** Trend in time of the pressures imposed at Σ_{PV} and Σ_{AR} for the three scenarios



heart [42], we employed the σ -LES method proposed for ventricular blood dynamics in [43] and successfully used in different hemodynamic applications [25, 44–46]. This turbulence model is suited to handle wall bounded flow in complex geometries, such as the ventricle [43].

In this framework, the displacement of LH $\mathbf{d}_{LH}^i(\mathbf{x})$ is derived in time and used to compute the wall velocity to prescribe it as boundary condition for the NS equations. However, $\mathbf{d}_{LH}^i(\mathbf{x})$ has been obtained only at the 30 MRI acquisition times, thus we performed a spline interpolation to obtain $\mathbf{d}_{LH}(\mathbf{x}, t)$ for all $t \in [0, T]$, where $T = 0.9 s$ is the duration of the heartbeat. According to the ALE framework, at each time, the fluid domain $\Omega(t)$ is obtained by extending $\mathbf{d}_{LH}(\mathbf{x}, t)$ into Ω through the solution of a linear elastic problem [47]. See [33] for further details.

In Fig. 4A, we displayed the fluid domain, where Σ_{LH} represents the internal wall surfaces of LH and Σ_{AR} and Σ_{PV} , the outlet and inlet sections of the aortic root and pulmonary veins, respectively. In yellow, we reported the aortic valve Γ_{AV} and in green, the mitral valve Γ_{MV} of the healthy subject. Thus, the ALE NS equations in the known domain $\Omega(t)$ are solved to find the blood pressure p and the blood velocity \mathbf{u} :

$$\begin{cases} \rho \left[\frac{\partial \mathbf{u}}{\partial t} + ((\mathbf{u} - \mathbf{u}_{ALE}) \cdot \nabla) \mathbf{u} \right] + (\mu_{sgs}(\mathbf{u}) + \mu) \Delta \mathbf{u} + \nabla p + \\ + \sum_{i=AV, MV} \frac{R_{\Gamma}}{\epsilon_{\Gamma}} (\mathbf{u} - \mathbf{u}_{ALE}) \delta_{\Gamma_i} = \mathbf{0} & \text{in } \Omega(t), \\ \nabla \cdot \mathbf{u} = 0 & \text{in } \Omega(t), \\ \mathbf{u} = \frac{\partial \mathbf{d}_{LH}}{\partial t} & \text{on } \Sigma_{LH}(t), \end{cases} \tag{1}$$

with a null initial condition in $\Omega(0)$. $\mu_{sgs}(\mathbf{u})$ is the sub-grid viscosity of the σ -model [43]; δ_{Γ_i} is a smoothed Dirac delta function representing a layer, with thickness $2\varepsilon_{\Gamma}$, around the surface of the valve Γ_i , $i = AV, MV$, [11, 41]; and R_{Γ} is a penalization term used to enforce the kinematic constraint. In our numerical simulations, we set $R_{\Gamma} = 10^5 \text{ kg/m} \cdot \text{s}$ and $\varepsilon_{\Gamma} = 0.75 \text{ mm}$ [14, 25, 33, 48, 49]. The position of the surface of each valve Γ_i , $i = AV, MV$, is updated at each time according to the valves displacement. In particular, for the AV case, since the displacement has been defined only in the open and closed configurations (see Fig. 2D), we multiplied $\mathbf{d}_{AV}(\mathbf{x})$ by a linear coefficient $C_{AV}(t)$, $t \in [0, T]$, equal to 0 when the valve is closed and 1 when it is opened. The opening and closing duration has been set according to the literature [50], i.e., 19 and 47 ms, for the opening and closing, respectively. Conversely, for MV, we did not need to make assumptions on the opening and closing times, since we reconstructed all the configurations from cine-MRI images. Thus, $\mathbf{d}_{MV}^t(\mathbf{x})$ has been directly interpolated in time to obtain $\mathbf{d}_{MV}(\mathbf{x}, t)$, $t \in [0, T]$.

Regarding the remaining boundary conditions of system (1), for all the three cases we prescribed a constant pressure of 10 mmHg on Σ_{PV} [51, 52] (Neumann condition on the normal direction) and a time-dependent physiological pressure taken from the Wiggers diagram [51, 53] at Σ_{AR} , see Fig. 4B. In the tangential direction, in order to avoid possible backflows instabilities, we prescribed a null velocity both on Σ_{PV} and Σ_{AR} [54].

To numerically solve system (1), we used *lifex* [55, 56] (<https://lifex.gitlab.io/>), a multiphysics high-performance C++ library based on the deal.II core [57]. In particular, we used first-order Finite Elements together with first-order semi-implicit discretization in time [58]. The numerical scheme was stabilized by means of the SUPG-PSPG scheme [59]. We run the simulations using 192 parallel processes on the GALILEO100 supercomputer (<https://www.hpc.cineca.it/hardware/galileo100>) at the CINECA high-performance computing center (Italy) allowing us to simulate a single heartbeat in about 16 h.

Tetrahedral mesh of the left heart was generated in VMTK with an average mesh element size of 0.9 mm and a local refinement in correspondence of the valves of 0.3 mm, see Fig. 3. The timestep Δt was equal to $5 \cdot 10^{-4} \text{ s}$. We performed a mesh convergence test ensuring that no significant differences may be found using a finer mesh or a smaller timestep. Furthermore, with this value of the average mesh element size, we are able to satisfy the Pope criterion used to assess the LES quality [60]. In particular, we computed the quantity $M(\mathbf{x}, t)$:

$$M(\mathbf{x}, t) = \frac{E_{\mu_{sgs}}(\mathbf{x}, t)}{(E_{\mu_{sgs}}(\mathbf{x}, t) + TKE(\mathbf{x}, t))}, \quad (2)$$

where $E_{\mu_{sgs}} = \mu_{sgs}(\mathbf{x}, t)^2 / (C \cdot h)^2$ [61] is the turbulent kinetic energy related to the unresolved scales, where $C = 1.5$ is the LES constant [43] and h is the local cell diameter; TKE is the turbulent kinetic energy of the resolved scales. Values of M below the threshold of 20% indicate that the LES is sufficiently resolved [27, 42, 60]. In our simulations, the average in time of the left ventricle volume with M below this threshold was about 80% for all the three scenarios, confirming that with such value of the average mesh element size we were able to capture, on average, 80% of the turbulent kinetic energy of the left ventricle. This result is in accordance with that found in other ventricular LES studies, see, e.g., [25, 27, 42].

Quantities of Interest

We computed the ensemble velocity (i.e., the average calculated over 9 heartbeats) and to compare and quantify the effects of the two repair techniques on the ventricular flow we introduced the following post-processed quantities:

- *Flow Stasis (FS)*: it is a function of space representing the percentage of the heartbeat during which the velocity magnitude is smaller than 0.1 m/s. Indeed, as suggested in [62–64], high FS values in correspondence of the ventricular apex (the area located at lower part or pointed end of the left ventricle, see Fig. 10, top) may suggest the aptitude of blood to stagnate and increase the risk of thrombus formation. FS is defined as follows:

$$FS(\mathbf{x}) = \frac{1}{T} \int_0^T \chi_{\{|\tilde{\mathbf{u}}(\mathbf{x}, t)| < 0.1 \text{ m/s}\}}(\mathbf{x}, t) dt,$$

where $\chi_{\{S\}}$ is the characteristic function which assumes value 1 if S is true, 0 otherwise, and $\tilde{\mathbf{u}}(\mathbf{x}, t)$ is the ensemble velocity;

- *Turbulent Kinetic Energy (TKE)*: at each time and space quantifies the velocity fluctuations by means of the fluid Reynolds stress tensor [27, 42]. High values of TKE in the ventricle are related to greater velocity fluctuations between heartbeats [27, 42] and with a non-physiological increased ventricular effort [27, 31]. TKE is defined as follows:

$$TKE(\mathbf{x}, t) = \frac{\rho}{2N} \sum_{j=1}^N \left((\tilde{u}_x(t + (j-1)T, \mathbf{x}) - u_x(t, \mathbf{x}))^2 + (\tilde{u}_y(t + (j-1)T, \mathbf{x}) - u_y(t, \mathbf{x}))^2 + (\tilde{u}_z(t + (j-1)T, \mathbf{x}) - u_z(t, \mathbf{x}))^2 \right),$$

where N is the number of the heartbeats (9 in our numerical experiments) and $\mathbf{u}(t, \mathbf{x})$ is the instantaneous velocity;

- *Vorticity*: at each time and space quantifies the amount of rotational behavior of blood flow [27, 42]. Together with turbulence, it allows to quantify the disturbed flow developed in the heart chambers. Vorticity is defined as the curl of the ensemble velocity field: $\nabla \times \tilde{\mathbf{u}}$;
- *Transversal pressure drop* $\Delta P_{transversal}$: defined as the pressure difference evaluated across a transverse direction within the ventricle: $P_r - P_\ell$, where P_r and P_ℓ are the pressure values in two points at the same distance from the apex, located in the right and left part of the chamber, respectively. When this pressure drop is large, it could indicate that the ventricle is experiencing more stress in one direction compared to the other one, potentially due to factors like disturbed flow patterns. This imbalance in stress distribution within the ventricle over time could influence the remodeling process, leading to, in the worst scenario, to abnormal dilation of the heart [31];
- *Turbulent force* τ_{max} (obtained from the fluid Reynolds stress tensor [65]): it is a function of space and time quantifying the fluctuating (turbulent) forces exerted among the fluid layers over the heartbeats as a consequence of the motion regime. τ_{max} has the following expression:

$$\tau_{max} = \frac{\rho}{2}(S_1 - S_3),$$

where $S_1 > S_3$ are the principal values of the Reynolds stress tensor $R_{ij} = u'_i u'_j$, with $\mathbf{u}' = \mathbf{u} - \tilde{\mathbf{u}}$. Values exceeding 800 Pa are recognized as condition that can damage the red blood cells promoting hemolysis [65].

Results

In Fig. 5, top, we reported the geometries and the displacement magnitude $\mathbf{d}_{MV}^i(\mathbf{x})$, together with arrows pointing the anterior (red) and posterior (blue) leaflets, of the reconstructed mitral valves of H, N, and R, at four representative instants. The values of the displacement were calculated with respect to the initial systolic configuration at t1. Instead, in Fig. 5, bottom, we displayed the evolution in time of the mitral valve orifice area during the heartbeat in the three scenarios. The mitral valve orifice area was computed by projecting the mitral valve orifice onto its least square plane according to [66]. We observed that at t2 all three scenarios featured a comparable orifice area, whereas at the peak of diastasis t3, R had a smaller area due to lesser posterior leaflet mobility. Conversely, at t4, the two patients who underwent surgery experienced a larger orifice area than H. Notice that the healthy subject H at t4 experienced only a partial opening of the mitral valve (specifically, only the middle part of the anterior leaflet underwent to a partial

reopening). This explain why the leftover part of the anterior leaflet remains in the same position as in previous frames.

In Fig. 6, we reported a longitudinal slice with the spatial distribution of the ensemble velocity magnitude at three instants for each scenario. At the peak of the E-wave t2, we observed comparable velocities across the mitral valve in all the scenarios with the formation of two ventricular vortex rings below the leaflets. However, in R, the mitral jet is oriented more toward the apex, while in scenarios H and N, the jet develops more along the ventricular wall. Additionally, we noticed in N and R the formation of a clockwise vortex in correspondence of the apex. At the peak of diastasis t3, we noticed a uniform clockwise vortex in H and N in the middle of the ventricle, whereas in R more swirling and chaotic structures were present. At the peak of A-wave t4, during the second injection of fluid in the ventricle, the velocities through MV in all the scenarios were too low to reach the middle of the ventricle, where the vortexes formed during diastasis were still present.

In Fig. 7, we reported the spatial distribution of the ensemble pressure together with the ensemble velocity patterns at the peak of the E-wave for the three scenarios. For H and N, the pressure appears to be the same and homogeneous in the atrium and in the ventricle, whereas in R, a negative pressure (reaching values up to -5 mmHg) is developing in the middle of the ventricle due to the presence of more pronounced eddies below the MV leaflets (cfr Fig. 6).

In Fig. 8, top, we reported the pressure drops evaluated between spheres placed in the transversal and longitudinal (trans-valvular) directions. The first one is significant to analyze possible remodeling of the ventricle [31], whereas the second is standard clinical measure to assess the functioning of the mitral valve. In both the cases we noticed that H and N exhibited a comparable pattern, whereas R displayed slightly larger oscillating values during the E-wave. This is particularly evident for the trans-valvular pressure drop, see also Fig. 7. In Table 2, for each scenario, we reported the average in time (during diastole) of the two pressure drops. We observed results very similar to the healthy case for both repair techniques in the transversal direction, whereas in the trans-valvular direction, the Resection technique exhibits larger values if compared with the healthy case and the Neochordae technique.

In Fig. 9, we reported on a selected longitudinal slice the spatial distribution of the amount of vorticity along the direction perpendicular to the slice at the peak of E-wave t2 and at the peak of diastasis t3. Positive values of the vorticity represent a clockwise direction of the vortexes. In the same figure, we also plotted TKE at the same time instants. We noticed that at t2 all the three scenarios exhibited a similar pattern with two vortex rings developing along the two mitral leaflets characterized by opposite directions. Moreover, the largest values of TKE were found right below the

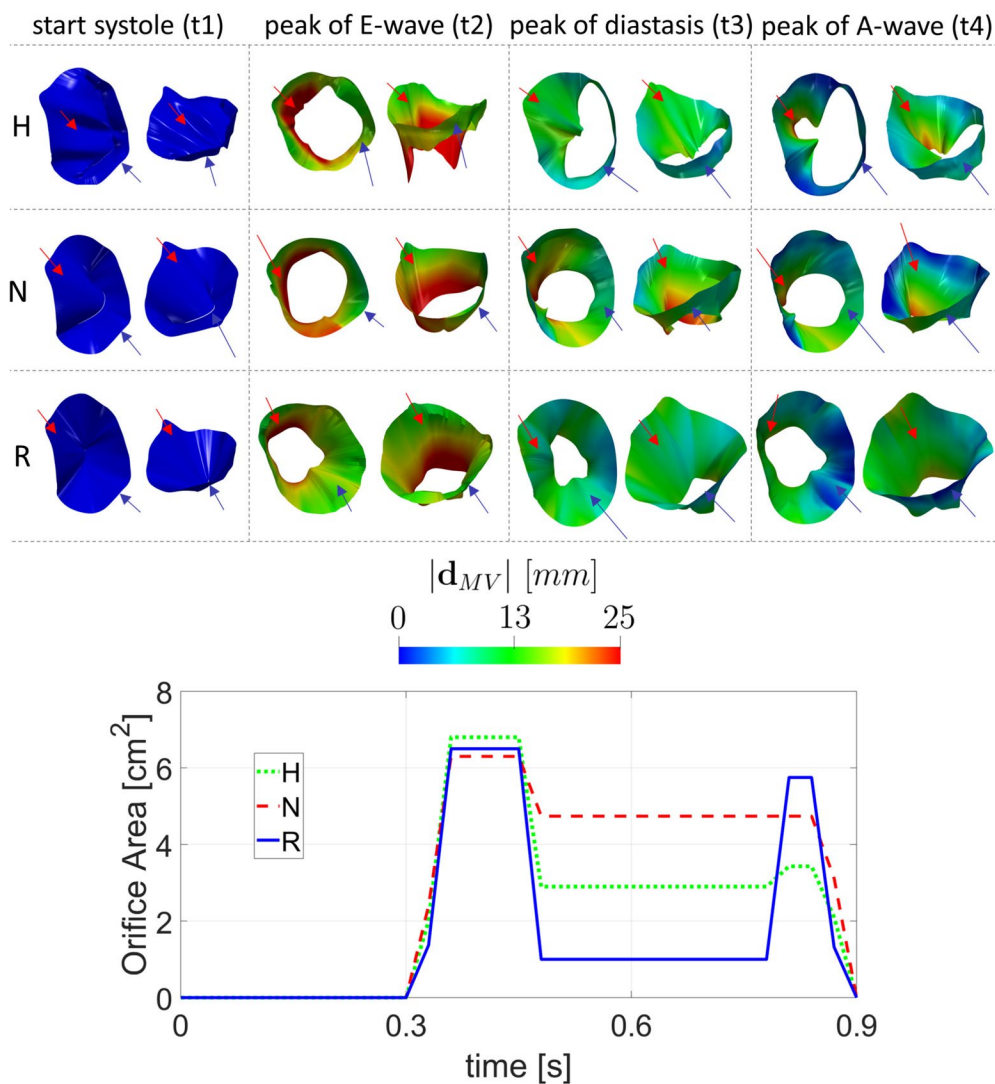


Fig. 5 Top: For each scenario (Healthy-H, Neochordae-N, and Resection-R) and for each box, we reported, for two different views, the geometries where the magnitude of the reconstructed cine-MRI displacement of the three mitral valve configurations $\mathbf{d}_{MV}(\mathbf{x})$ is plotted at (see Fig. 2C): the begin of systole t1, the peak of flow rate during E-wave t2, the instant t3 of maximum ventricular flow rate dur-

ing diastasis, and the instant t4 of maximum valve opening during the A-wave. The displacement was calculated with respect to the start-systolic configuration; the arrows indicate the two leaflets: red for the anterior; blue for the posterior one. Bottom: Evolution in time of the mitral valve orifice area during the heartbeat in the three scenarios

anterior leaflet. Furthermore, we observed the existence of turbulent regions in correspondence of the apex especially in R, attributed to the presence of pronounced eddies, see also Fig. 6. At t3, we observe a significant, well-defined clockwise vortex in the center of the ventricle for H and N, whereas for R multiple disorganized vortices were found. This led to high values of TKE for R, concentrated in the LVOT and in the central region of the ventricle. This suggests that Resection technique induces more pronounced fluctuations in velocity values across the heartbeats compared to other the other two cases. In Fig. 8, middle, we reported the trend in time of the Global Turbulent Kinetic Energy (GTKE, i.e., TKE integrated over the ventricle)

during the diastolic phase. Notice the large values featured by R especially during diastasis, whereas similar slightly lower values were observed for H and N. This results are in accordance with the average values reported in Table 2. In the same figure, we reported also GTKE values obtained as the average among several healthy cases with 4D flow MRI [67], highlighting very similar values for what we found in the H scenario.

In Fig. 10, we reported some quantities useful in view of a clinical analysis, such as the capability of washing out the ventricular apex and the hemolysis formation. Specifically, in the top figure, we reported the spatial distribution of the Flow Stasis (FS) in the ventricular apex, where maximum

Fig. 6 Magnitude of the ensemble velocity computed over 9 heartbeats at t2 (peak E-wave), t3 (peak of diastasis), and t4 (peak of A-wave) for the three scenarios Healthy (H), Neochordae (N), and Resection (R)

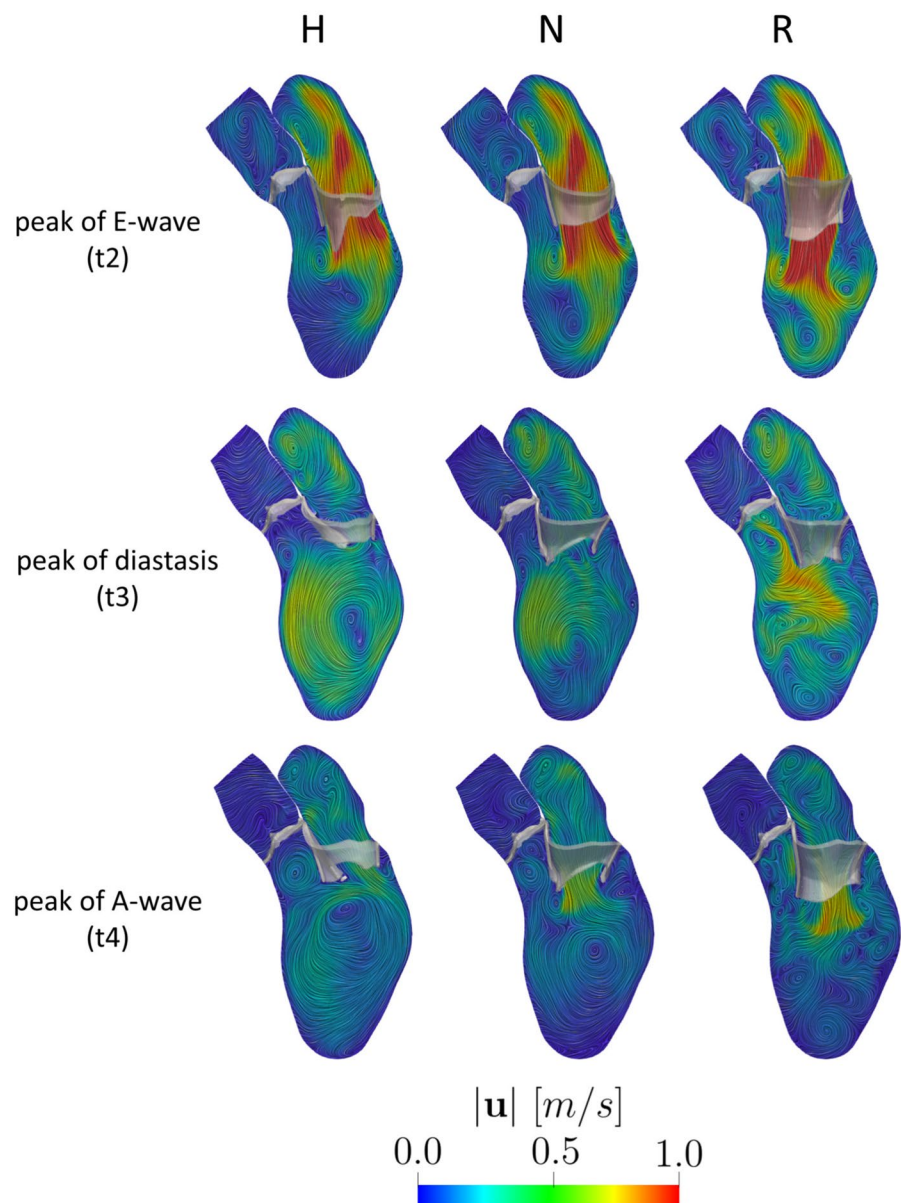


Table 2 Values of the quantities of interest computed for each scenario. $\overline{\Delta P}_{transversal}$: average in time of the pressure drop evaluated between the ventricular septum and free wall during the diastolic phase; $\overline{\Delta P}_{longitudinal}$ average in time of the pressure drop evaluated between the ventricular base and apex during the diastolic phase;

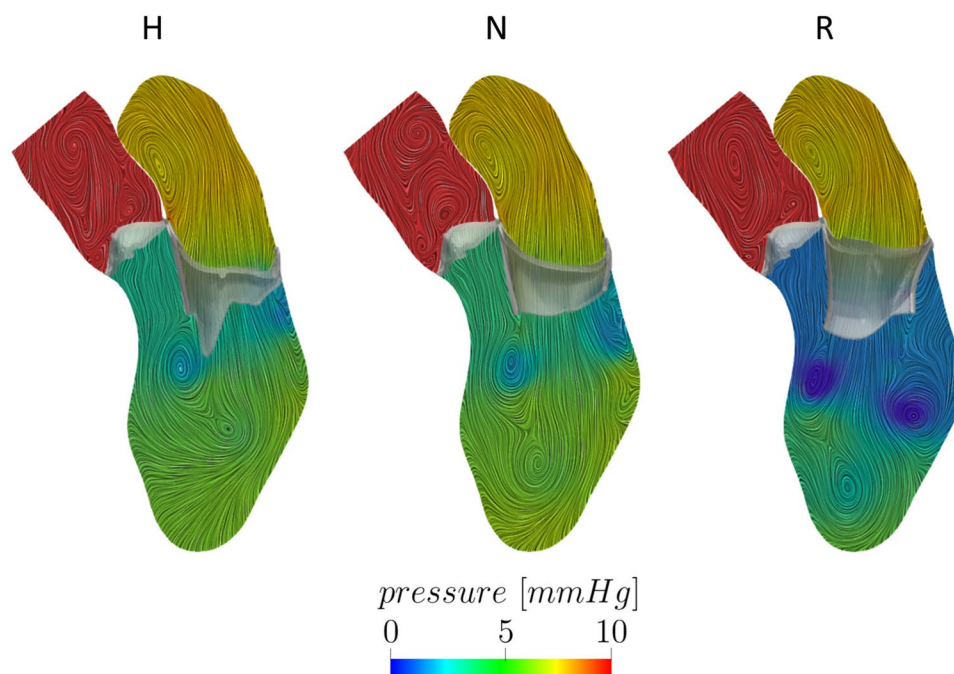
Scenario	$ \overline{\Delta P}_{transversal} $ [mmHg]	$\overline{\Delta P}_{trans-valvular}$ [mmHg]	$\overline{GTKE}_{diastole}$ [mJ]	$FS(\mathbf{x}) > 80\%$ [%]	$\overline{\tau_{max,diastole}}$ [Pa]
H	0.11	1.7	0.9	31	6.7
N	0.17	1.9	0.8	48	6.2
R	0.08	3.6	1.1	15	7.8

$\overline{GTKE}_{diastole}$: average in time of GTKE evaluated in the ventricle during the diastolic phase; Percentage of volume with $FS(\mathbf{x})$ greater than 80% evaluated in the ventricular apex; and $\overline{\tau_{max,diastole}}$: average in time of τ_{max} evaluated in the ventricle during the diastolic phase. Scenarios: Healthy (H), Neochordae (N), and Resection (R)

values are attained. Notice that, for the FS computation, we consider a region starting from the ventricular apex and extending 1 cm toward the mitral valve, see the black box

in Fig. 10, top. We can observe that R features lower values of FS than H and N cases. To quantify these differences, we reported in Table 2 the percentage of volume of interest

Fig. 7 Spatial distribution of the ensemble pressure computed over 9 heartbeats with the ensemble velocity patterns in background at the peak of the E-wave t_2 for the three scenarios Healthy (H), Neochordae (N), and Resection (R)



with FS greater than a representative threshold of 80%. This suggests a possible better ability of R to washout ventricular blood in the apex with respect to H and, especially, to N. Notice that the analysis performed with other values of the threshold led to the same conclusions (percentage of area below the threshold lower in R). Moreover, the value of the distance of 1 cm from the ventricular apex has been considered as a representative value to differentiate the impacts of the three scenarios (H, N, and R) on FS. Nevertheless, additional analysis conducted using other offset values led us to the same conclusions (percentage of FS below 80% was lower in R).

In Fig. 10, bottom, we reported the spatial distribution of the turbulent forces τ_{max} in a region of interest around the mitral valve during its opening. We noticed that, even if none of the three scenarios exceeded the critical threshold of 800 Pa [65], R gives rise to values up to 640 Pa (just below the mitral orifice), whereas H and N featured maximum values of 210 and 230 Pa, respectively. Accordingly, in Fig. 8, bottom, we reported during the diastolic phase the evolution in time of the average τ_{max} within the ventricle. We notice that R featured larger values during the mitral opening than H and N, which displayed a similar trend. This is in accordance with the τ_{max} distribution at the valve opening reported in Fig. 10, bottom. Also, the values of average-in-space τ_{max} are larger for R during diastasis, in correspondence of elevated values of GTKE, see Fig. 8, middle. The time-average values of τ_{max} are reported in Table 2, confirming the significant attitude of R to develop large turbulent forces.

Discussion

In this work, we performed an image-based computational fluid dynamic study in the left heart to compare the hemodynamics associated with two surgical reparative techniques (Neochordae and Resection) for the treatment of prolapse that may result in primary mitral regurgitation. To the best of the authors' knowledge, this is the first computational study aiming to investigate the blood dynamics in presence of different mitral valve reparative techniques.

We point out that our study utilizes advanced cine-MRI images specific to the mitral valve. However, possible uncertainties in mitral leaflets segmentation during some frames of the heartbeat may be present. Indeed, its rapid and millimeter-thin structure makes difficult to fully recognize the leaflet profiles at some MRI plane.

Despite these challenges, we believe that the results evaluated in the two scenarios analyzed may have a significant clinical impact, especially when comparing the two repair techniques against the normal mitral valve (Healthy). In other words, the more similar are the hemodynamics (such as velocity, pressure, vorticity patterns) of the repaired mitral valves to the normal one, the more physiological the hemodynamics will be and, in turn, the more complete the LV remodeling may possibly be. This could give useful clinical indications to cardio-surgeons in view of the choice of the reparation technique. In this direction, we first notice that at the peak of diastasis t_3 , R has a smaller area due to lesser posterior leaflet mobility, which is a typical finding in the Resection technique [4]. A smaller

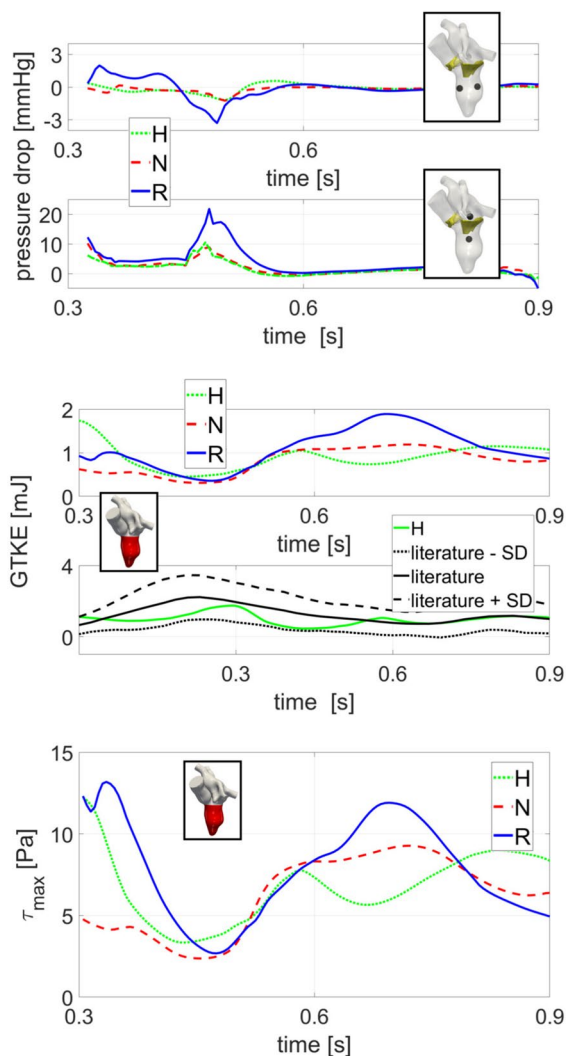


Fig. 8 Top: Evolution in time, during diastole, of the pressure drops in the transversal and trans-valvular directions; Middle: Evolution in time of GTKE integrated over the left ventricle volume during the diastolic phase (top) and comparison with respect to an average reference [67] (bottom); Bottom: Evolution in time of τ_{max} integrated over the left ventricle volume (bottom). Scenarios: Healthy (H), Neochordae (N), and Resection (R)

area translates clinically into a worse LV performance. In fact, a restrictive area after a mitral valve repair is considered a technical failure [68]. This mainly influences the behavior of the diastolic jet during the E-wave, which is directed in case of the Resection technique more toward the apex than in the other two cases, see Fig. 6. On the contrary, the Neochordae technique features a diastolic jet more similar to the healthy case in terms of direction (developing more toward the ventricle wall) and vortexes formation, see Figs. 6 and 9. The pattern velocity is almost overlapping in H and N, meaning that there is a more physiological pattern in H potentially leading to a better clinical outcome and a more proficient LV remodeling. The different direction of the jet

allows blood in the Resection technique to reach the apex more quickly and with more pronounced washout compared to the other two cases. This is confirmed by the analysis performed on the Flow Stasis quantity (see Fig. 10, top and Table 2), suggesting that the Resection technique may provide a greater protective role from potential thrombi formation [69].

The analysis of the pressure drops (Fig. 8, top and Table 2) highlighted that within the ventricle the three scenarios exhibited comparable temporal evolutions (see Fig. 8, top) and time-average values (see Table 2) and thus that the two operations lead to physiological values. As a consequence, according to the literature [31], the two techniques should not promote a non-physiological ventricular remodeling, characterized by a ventricle dilation which may occur in response to abnormal loading (pressure) conditions. From the analysis on the trans-valvular pressure drop we noticed that, although the Resection technique exhibited a time-average value twofold greater than in the other cases (see Table 2), its trans-valvular pressure drop falls within the physiological range (0–5 mmHg) [70]. This suggests that both techniques ensure a proper mitral functioning during diastole.

The vorticity analysis highlighted that during the E-wave, the Neochordae and Resection techniques showed a rotational behavior of the blood flow comparable to that of the healthy case. Specifically, all the scenarios are characterized by two different vortexes developing below the leaflets, see Fig. 9, top. However, during diastasis, Resection technique amplifies the rotational dynamics of the blood and multiple and non-coherent eddies develop (see Figs. 6 and 9, bottom). Instead, the Neochordae technique and the healthy scenario featured during diastasis the standard clockwise vortex in the middle of the ventricle, see Fig. 9, bottom. The different behaviors featured by the Resection technique at diastasis are mainly attributed to the reduced mobility of the posterior leaflet. This produces a jet which is directed (unlike the other two cases) toward the apex. As a consequence, according to the literature [30, 31], Resection technique may promote a non-physiological intracardiac vortex dynamics that may affect the heart efficiency, resulting in the worst scenario to heart failure. Furthermore, the analysis of the vorticity (see Fig. 9) seems to reinforce the concept that the Neochordae technique has a more physiological impact on the fluid dynamics of the LV which positively reflects on hemodynamic performance, remodeling process, and potentially on a longer durability of the repair.

We observed that there exists a relationship between areas with large vorticity and areas with high turbulence formation, see Fig. 9. In particular, although the time evolution and average values of the three scenarios are comparable (see Fig. 8, middle and Table 2), during diastasis there is much more turbulence formation in the Resection

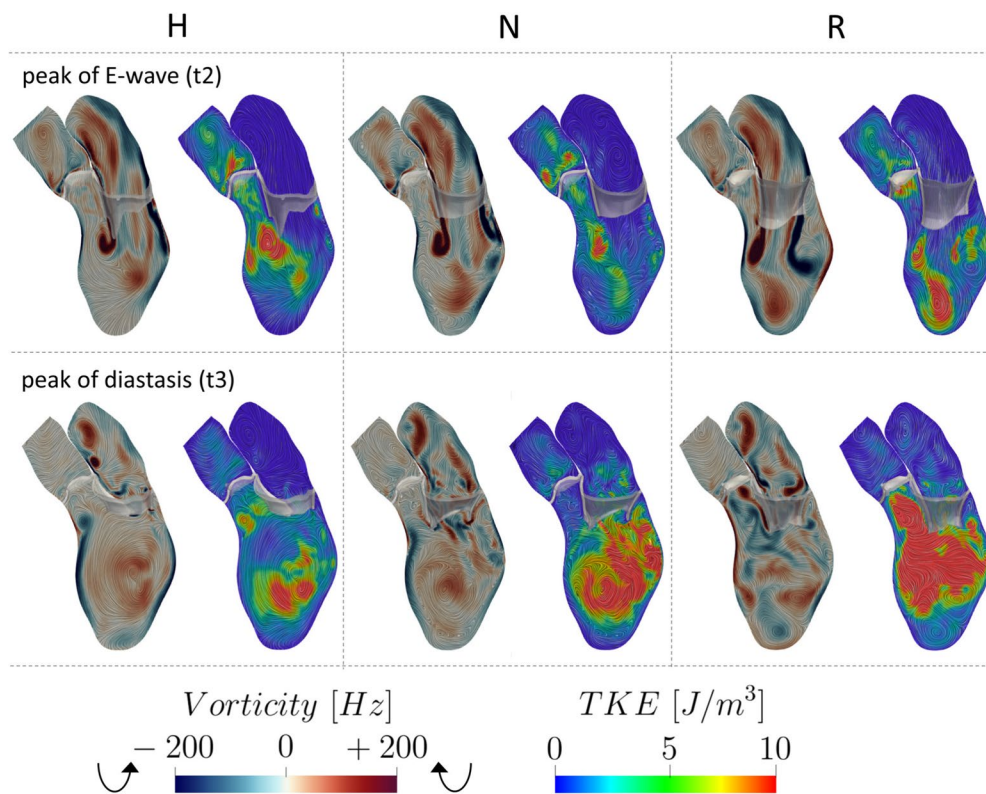


Fig. 9 Spatial distribution of the vorticity and TKE at the peak of E-wave t_2 and peak of diastasis t_3 , for the three scenarios Healthy (H), Neochordae (N), and Resection (R)

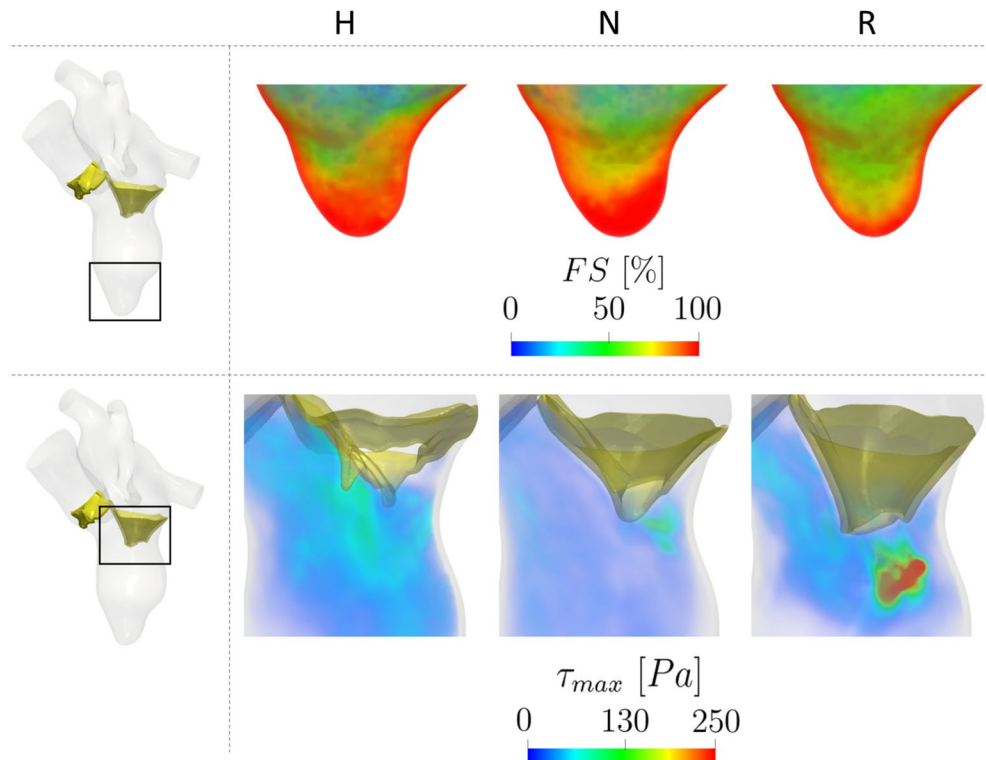


Fig. 10 Top: Spatial distribution of FS (\mathbf{x}) in correspondence of the ventricular apex. Bottom: Spatial distribution of τ_{max} in correspondence of the mitral valve during its opening. Scenarios: Healthy (H), Neochordae (N), and Resection (R)

technique, due to the presence of several ventricular swirling structures, see also Fig. 6. As a consequence, according to the literature [31], the presence of pronounced fluctuations in the Resection technique may contribute to increase the ventricular effort during the heartbeat.

According to the definition of τ_{max} (see Sect. 2.3), turbulence may create the conditions also for hemolysis development, a phenomenon related to the destruction of red blood cells due to fluid forces. According to [65], values of τ_{max} exceeding 800 Pa are identified as conditions that may induce hemolysis. Our findings reveal that the Resection technique significantly approaches this threshold during the mitral opening. This may indicate that a pronounced hypo-mobility of the posterior leaflet experienced by the Resection technique could result in the creation of turbulent forces capable of causing damage to red blood cells, thus promoting hemolysis which represents a potential cause of failure in mitral valve repair [71].

We point out that all the results in this study have been obtained under the assumption that both repair techniques yield to the same ventricular displacement of the healthy subject. This assumption holds true for those post-operative scenarios that follow a pre-operative condition characterized by an almost physiological myocardial displacement. This is the case, for example, of prolapse not resulting in regurgitation or if the operation occurs during the early stages of mitral regurgitation [72, 73]. Specifically, our two operated cases were characterized by no regurgitation of the prolapse. In accordance, we did not focus our attention on processing our results in the left atrium, since during diastole the blood dynamics is therein not relevant in terms of differences about the scenarios.

Accordingly, the two operated mitral valves were virtually inserted and adapted in the left heart of the healthy subject by preserving the ratio between the area of the annulus and the area of the mitral orifice measured for the patients from imaging at the peak of the E-wave. We believe that this could be a well-accepted strategy if one wants to compare the effect of only one change (in our case the mitral valve geometry) on the output of interest (see, e.g., [53] for the case of mitral valve prolapse, [11] for different systolic anterior motion degrees, [24] for a structural analysis of the comparison of the two reparative techniques).

Limitations

Some limitations characterized this work:

- (1) We considered only two operated patients and one healthy subject. This was a consequence of the fact that we used advanced (not daily available) images of the mitral valve in order to perform highly accurate DIB-

CFD simulations. However, we point out that this was not a statistical study, rather we wanted to describe the physical processes underlying blood dynamics of mitral repaired patients. Anyway, we are well aware that the small number of cases examined will require further validations by larger series. However, the rationale behind this study is to give, for the first time to the best of our knowledge, a scientific and mathematical foundation to the clinical idea that the so-called “respect technique” is more physiological than the repair technique, entailing leaflet resection, originally proposed by Alain Carpentier [1].

- (2) We did not include the papillary muscles in the ventricle geometry. This is a common choice in computational studies, adopted also in [11, 26, 74–76], due to the difficulty to reconstruct them from MRI images. Nevertheless, although our outcomes seem to be in accordance with previous studies, their influence on the quantities of interest could be relevant and it will be the subject of future studies;
- (3) We did not consider the chordae tendineae. This may be of particular relevance for the Neochordae technique. However, for this comparison study, we believed that this common choice should not affect the qualitative conclusions on the two operated scenarios too much.
- (4) Our mesh did not include any boundary layer to better capture the blood dynamic behavior close to the myocardial wall. This should be considered in future studies. However, we noticed that our mesh resolution obtained after a refinement study was able to satisfy the Pope criterion [60].

Conclusion

In conclusion, our results underlined that the Resection technique seems to give rise to a diastolic jet pointing more toward the apex than those developed by the healthy case and the Neochordae technique. This increases the capability to protect the ventricular apex from potential thrombi formation, but at the same time promotes turbulence formation and chaotic and swirling eddies, which increase ventricular effort and risk of hemolysis. Conversely, the Neochordae technique exhibits patterns of velocities, turbulence, and vorticity that are more similar to those observed in the healthy scenario. Therefore, according to our preliminary results, the Neochordae technique seems to represent the best option to restore and maintain a physiological ventricular fluid dynamics.

Acknowledgements The authors acknowledge the CINECA award under the ISCRA C initiatives, for the availability of high-performance computing resources and support (IsCa8_DIB-CFD, P.I.

Lorenzo Bennati, 2023), and the INdAM - GNCS Project CUP_E53C22001930001 (P.I. Stefano Pagani, 2023).

LB and CV are members of the INdAM group GNCS “Gruppo Nazionale per il Calcolo Scientifico” (National Group for Scientific Computing). CV has been partially supported by the Italian Ministry of University and Research (MIUR) within the PRIN (Research projects of relevant national interest) MIUR PRIN22-PNRR n. P20223KSS2 “Machine learning for fluid–structure interaction in cardiovascular problems: efficient solutions, model reduction, inverse problems, and by the Italian Ministry of Health within the PNC PROGETTO HUB - DIAGNOSTICA AVANZATA (HLS-DA) “INNOVA,” PNC-E3-2022-23683266”.

Author Contributions Acquisition of the clinical data: GP. Methodology: LB and CV. Image Reconstruction and numerical simulations: LB. Conceptualization: LB, GP, VG, GBL, and CV. Formal analysis and investigation: LB. Interpretation of the results: LB and CV. Writing - Original draft preparation: LB. Writing - Review and editing: CV, GP, VG, and GBL. Supervision: CV and GBL.

Funding Open access funding provided by Politecnico di Milano within the CRUI-CARE Agreement.

Declarations

Conflict of interest No conflict of interest, financial, or otherwise are declared by the authors.

Ethical Approval Ethical review board approval and informed consent were obtained from all patients.

Open Access This article is licensed under a Creative Commons Attribution 4.0 International License, which permits use, sharing, adaptation, distribution and reproduction in any medium or format, as long as you give appropriate credit to the original author(s) and the source, provide a link to the Creative Commons licence, and indicate if changes were made. The images or other third party material in this article are included in the article’s Creative Commons licence, unless indicated otherwise in a credit line to the material. If material is not included in the article’s Creative Commons licence and your intended use is not permitted by statutory regulation or exceeds the permitted use, you will need to obtain permission directly from the copyright holder. To view a copy of this licence, visit <http://creativecommons.org/licenses/by/4.0/>.

References


1. Carpentier, A. Cardiac valve surgery—the “french correction”. *The Journal of Thoracic and Cardiovascular Surgery*. 86(3):323–337, 1983. [https://doi.org/10.1016/S0022-5223\(19\)39144-5](https://doi.org/10.1016/S0022-5223(19)39144-5).
2. Johnston, D. R., A. M. Gillinov, E. H. Blackstone, B. Griffin, W. Stewart, J. F. Sabik III., T. Mihaljevic, L. G. Svensson, P. L. Houghtaling, and B. W. Lytle. Surgical repair of posterior mitral valve prolapse: Implications for guidelines and percutaneous repair. *The Annals of Thoracic Surgery*. 89(5):1385–1394, 2010. <https://doi.org/10.1016/j.athoracsur.2009.12.070>.
3. Chemtob, R. A., P. Wierup, S. Mick, and M. Gillinov. Choosing the “best” surgical techniques for mitral valve repair: Lessons from the literature. *Journal of Cardiac Surgery*. 34(8):717–727, 2019. <https://doi.org/10.1111/jocs.14089><https://onlinelibrary.wiley.com/doi/pdf/10.1111/jocs.14089>
4. Perier, P., W. Hohenberger, F. Lakew, and A. Diegeler. Prolapse of the posterior leaflet: resect or respect. *Ann Cardiothorac Surg*. 4(3):273–277, 2015.
5. Tirone, D. Replacement of chordae tendineae with expanded polytetrafluoroethylene sutures. *Journal of Cardiac Surgery*. 4(4):286–290, 1989. <https://doi.org/10.1111/j.1540-8191.1989.tb00291.x>.
6. Tirone, D. Artificial chordae. *Seminars in Thoracic and Cardiovascular Surgery*. 16(2):161–168, 2004. <https://doi.org/10.1053/j.semtevs.2004.03.004>.
7. Hysi, I., O. Rebet, L. Gautier, and O. Fabre. A standardized loop technique for mitral valve repair. *The Annals of Thoracic Surgery*. 103(1):105–106, 2017. <https://doi.org/10.1016/j.athoracsur.2016.06.104>.
8. Salvador, L., S. Mirone, R. Bianchini, T. Regesta, F. Patelli, G. Minniti, M. Masat, E. Cavarretta, and C. Valfrè. A 20-year experience with mitral valve repair with artificial chordae in 608 patients. *The Journal of Thoracic and Cardiovascular Surgery*. 135(6):1280–1287, 2008. <https://doi.org/10.1016/j.jtcvs.2007.12.026>.
9. Esmaily, M., A. Kahn, E. Tseng, J. Guccione, and A. Marsden. Patient-specific multiscale modeling of blood flow for coronary artery bypass graft surgery. *Annals of Biomedical Engineering*. 40:2228–42, 2012. <https://doi.org/10.1007/s10439-012-0579-3>.
10. Cao, K., and P. Sucaskey. Computational comparison of regional stress and deformation characteristics in tricuspid and bicuspid aortic valve leaflets. *International Journal for Numerical Methods in Biomedical Engineering*. 33(3):02798, 2017. <https://doi.org/10.1002/cnm.2798>.
11. Fumagalli, I., M. Fedele, C. Vergara, L. Dede’, S. Ippolito, F. Nicolò, C. Antona, R. Scrofani, and A. Quarteroni. An image-based computational hemodynamics study of the systolic anterior motion of the mitral valve. *Computers in Biology and Medicine*. 123:103922, 2020. <https://doi.org/10.1016/j.combiomed.2020.103922>.
12. Viola, F., V. Spandan, V. Meschini, J. Romero, M. Fatica, M. D. de Tullio, and R. Verzicco. FSEI-GPU: GPU accelerated simulations of the fluid-structure-electrophysiology interaction in the left heart. *Computer Physics Communications*. 273:108248, 2022. <https://doi.org/10.1016/j.cpc.2021.108248>.
13. Caballero, A., W. Mao, R. McKay, and W. Sun. Transapical mitral valve repair with neochordae implantation: FSI analysis of neochordae number and complexity of leaflet prolapse. *International Journal for Numerical Methods in Biomedical Engineering*. 36(3):3297, 2020. <https://doi.org/10.1002/cnm.3297>.
14. Zingaro, A., I. Fumagalli, L. Dede, M. Fedele, P. C. Africa, A. F. Corno, and A. Quarteroni. A geometric multiscale model for the numerical simulation of blood flow in the human left heart. *Discrete and Continuous Dynamical Systems*. 2022. <https://doi.org/10.3934/dcds.2022052>.
15. Spühler, J. H., J. Jansson, N. Jansson, and J. Hoffman. 3D fluid-structure interaction simulation of aortic valves using a unified continuum ALE FEM model. *Frontiers in Physiology*. 2018. <https://doi.org/10.3389/fphys.2018.00363>.
16. Luraghi, G., F. Migliavacca, A. García, C. Chiastra, A. Rossi, D. Cao, G. Stefanini, and J. Rodriguez. On the modeling of patient-specific transcatheter aortic valve replacement: A fluid-structure interaction approach. *Cardiovascular Engineering and Technology*. 10:1–19, 2019. <https://doi.org/10.1007/s13239-019-00427-0>.
17. Fumagalli, I., R. Polidori, F. Renzi, L. Fusini, A. Quarteroni, G. Pontone, C. Vergara. Fluid-structure interaction analysis of transcatheter aortic valve implantation. MOX Report n* 29/2022, Dipartimento di Matematica, Politecnico di Milano (2022)
18. Gallo, D., U. Morbiducci, and M. D. de Tullio. On the unexplored relationship between kinetic energy and helicity in prosthetic heart valves hemodynamics. *International Journal of Engineering Science*. 177:103702, 2022. <https://doi.org/10.1016/j.ijengsci.2022.103702>.
19. Carbonaro, D., D. Gallo, U. Morbiducci, A. Audenino, and C. Chiastra. In silico biomechanical design of the metal frame of transcatheter aortic valves: multi-objective shape and

- cross-sectional size optimization. *Structural and Multidisciplinary Optimization*. 64(4):1825–1842, 2021. <https://doi.org/10.1007/s00158-021-02944-w>.
20. Rim, Y., A. Choi, D. D. McPherson, and H. Kim. Personalized computational modeling of mitral valve prolapse: Virtual leaflet resection. *PLoS ONE*. 10(6):1–15, 2015. <https://doi.org/10.1371/journal.pone.0130906>.
 21. Sturla, F., F. Onorati, E. Votta, K. Pechlivanidis, M. Stevanella, A. D. Milano, G. Puppini, A. Mazzucco, A. Redaelli, and G. Fagian. Is it possible to assess the best mitral valve repair in the individual patient? preliminary results of a finite element study from magnetic resonance imaging data. *The Journal of Thoracic and Cardiovascular Surgery*. 148(3):1025–1034, 2014. <https://doi.org/10.1016/j.jtcvs.2014.05.071>.
 22. Reimink, M. S., K. S. Kunzelman, and R. P. Cochran. The effect of chordal replacement suture length on function and stresses in repaired mitral valves: a finite element study. *J Heart Valve Dis*. 5(4):365–375, 1996.
 23. Di Micco, L., P. Peruzzo, A. Colli, G. Burriesci, D. Boso, L. Besola, G. Gerosa, and F. M. Susin. The neochoord mitral valve repair procedure: Numerical simulation of different neochoords tensioning protocols. *Medical Engineering & Physics*. 74:121–128, 2019. <https://doi.org/10.1016/j.medengphy.2019.09.014>.
 24. Choi, A., D. D. McPherson, and H. Kim. Neochoordoplasty versus leaflet resection for ruptured mitral chordae treatment: Virtual mitral valve repair. *Computers in Biology and Medicine*. 90:50–58, 2017. <https://doi.org/10.1016/j.compbiomed.2017.09.006>.
 25. Bennati, L., V. Giamb Bruno, F. Renzi, V. Di Nicola, C. Maffei, G. Puppini, G. B. Luciani, and C. Vergara. Turbulent blood dynamics in the left heart in the presence of mitral regurgitation: a computational study based on multi-series cine-mri. *Biomechanics and Modeling in Mechanobiology*. 2023. <https://doi.org/10.1007/s10237-023-01735-0>.
 26. Fumagalli, I., P. Vitullo, C. Vergara, M. Fedele, A. F. Corno, S. Ippolito, R. Scrofani, and A. Quarteroni. Image-based computational hemodynamics analysis of systolic obstruction in hypertrophic cardiomyopathy. *Frontiers in Physiology*. 2022. <https://doi.org/10.3389/fphys.2021.787082>.
 27. Chnafa, C., S. Mendez, and F. Nicoud. Image-based simulations show important flow fluctuations in a normal left ventricle: What could be the implications? *Annals of Biomedical Engineering*. 44(11):3346–3358, 2016. <https://doi.org/10.1007/s10439-016-1614-6>.
 28. Seo, J. H., V. Vedula, T. Abraham, A. Lardo, F. Dawoud, H. Luo, and R. Mittal. Effect of the mitral valve on diastolic flow patterns. *Physics of Fluids*. 26:121901, 2014. <https://doi.org/10.1063/1.4904094>.
 29. Vedula, V., R. George, L. Younes, and R. Mittal. Hemodynamics in the Left Atrium and Its Effect on Ventricular Flow Patterns. *Journal of Biomechanical Engineering*. 137(11):111003, 2015. <https://doi.org/10.1115/1.4031487>.
 30. Hong, G.-R., G. Pedrizzetti, G. Tonti, P. Li, Z. Wei, J.K. Kim, A. Baweja, S. Liu, N. Chung, H. Houle, J. Narula, M.A. Vannan. Characterization and quantification of vortex flow in the human left ventricle by contrast echocardiography using vector particle image velocimetry. *JACC: Cardiovascular Imaging* 1(6), 705–717 (2008) <https://doi.org/10.1016/j.jcmg.2008.06.008>
 31. Pedrizzetti, G., G. Canna, O. Alfieri, and G. Tonti. The vortex - an early predictor of cardiovascular outcome? *Nature reviews. Cardiology*. 2014. <https://doi.org/10.1038/nrcardio.2014.75>.
 32. Du Bois, D., E.F. Du Bois, A formula to estimate the approximate surface area if height and weight be known. 1916. *Nutrition* 5(5), 303–11 (1989)
 33. Bennati, L., C. Vergara, V. Giamb Bruno, I. Fumagalli, A. F. Corno, A. Quarteroni, G. Puppini, and G. B. Luciani. An image-based computational fluid dynamics study of mitral regurgitation in presence of prolapse. *Cardiovasc Eng Tech*. 2023. <https://doi.org/10.1007/s13239-023-00665-3>.
 34. Stevanella, M., F. Maffessanti, C. Conti, E. Votta, A. Arnoldi, M. Lombardi, O. Parodi, E. Caiani, and A. Redaelli. Mitral valve patient-specific finite element modeling from cardiac MRI: Application to an annuloplasty procedure. *Cardiovascular Engineering and Technology*. 2:66–76, 2011. <https://doi.org/10.1007/s13239-010-0032-4>.
 35. Antiga, L., M. Piccinelli, L. Botti, B. Ene-Iordache, A. Remuzzi, and D. A. Steinman. An image-based modeling framework for patient-specific computational hemodynamics. *Medical & Biological Engineering & Computing*. 46(11):1097–1112, 2008. <https://doi.org/10.1007/s11517-008-0420-1>.
 36. Fedele, M., and A. Quarteroni. Polygonal surface processing and mesh generation tools for the numerical simulation of the cardiac function. *International Journal for Numerical Methods in Biomedical Engineering*. 2021. <https://doi.org/10.1002/cnm.3435>.
 37. Quarteroni, A., R. Sacco, and F. Saleri. *Numerical Mathematics*, Vol. 37, Berlin: Springer, 2007. <https://doi.org/10.1007/b98885>.
 38. Quarteroni, A. *Numerical Models for Differential Problems*, Vol. 2, Berlin: Springer, 2013. <https://doi.org/10.1007/978-88-470-1071-0>.
 39. Donea, J., S. Giuliani, and J. P. Halleux. An arbitrary Lagrangian-Eulerian finite element method for transient dynamic fluid-structure interactions. *Computer Methods in Applied Mechanics and Engineering*. 33(1):689–723, 1982. [https://doi.org/10.1016/0045-7825\(82\)90128-1](https://doi.org/10.1016/0045-7825(82)90128-1).
 40. Fernández, Miguel A., Gerbeau, Jean-Frédéric, Martin, Vincent: Numerical simulation of blood flow through a porous interface. *ESAIM: M2AN* 42(6), 961–990 (2008) <https://doi.org/10.1051/m2an:2008031>
 41. Fedele, M., E. Faggiano, L. Dede, and A. Quarteroni. A patient-specific aortic valve model based on moving resistive immersed implicit surfaces. *Biomechanics and Modeling in Mechanobiology*. 16:1779–1803, 2017. <https://doi.org/10.1007/s10237-017-0919-1>.
 42. Chnafa, C., S. Mendez, and N. Franck. Image-based large-eddy simulation in a realistic left heart. *Computers & Fluids*. 94:173–187, 2014. <https://doi.org/10.1016/j.compfluid.2014.01.030>.
 43. Nicoud, F., H. Toda, O. Cabrit, S. Bose, and J. Lee. Using singular values to build a subgrid-scale model for large eddy simulation. *Physics of Fluids*. 2011. <https://doi.org/10.1063/1.3623274>.
 44. Lancellotti, R. M., C. Vergara, L. Valdettaro, S. Bose, and A. Quarteroni. Large eddy simulations for blood dynamics in realistic stenotic carotids. *International Journal for Numerical Methods in Biomedical Engineering*. 33(11):2868, 2017. <https://doi.org/10.1002/cnm.2868>.
 45. Vergara, C., D. Le Van, M. Quadrio, L. Formaggia, and M. Domanin. Large eddy simulations of blood dynamics in abdominal aortic aneurysms. *Medical Engineering & Physics*. 47:38–46, 2017. <https://doi.org/10.1016/j.medengphy.2017.06.030>.
 46. Stella, S., C. Vergara, L. Giovannacci, A. Quarteroni, and G. Prouse. Assessing the disturbed flow and the transition to turbulence in the arteriovenous fistula. *Journal of Biomechanical Engineering*. 2019. <https://doi.org/10.1115/1.4043448>.
 47. Stein, K., T. Tezduyar, and R. Benney. Mesh moving techniques for fluid-structure interactions with large displacements. *Journal of Applied Mechanics*. 70(1):58–63, 2003. <https://doi.org/10.1115/1.1530635>.
 48. Bucelli, M., A. Zingaro, P. C. Africa, I. Fumagalli, L. Dede, and A. Quarteroni. A mathematical model that integrates cardiac electrophysiology, mechanics, and fluid dynamics: Application to the human left heart. *International Journal for Numerical Methods in Biomedical Engineering*. 2023. <https://doi.org/10.1002/cnm.3678>.

49. Zingaro, A., M. Bucelli, R. Piersanti, F. Regazzoni, L. Dede', A. Quarteroni. An electromechanics-driven fluid dynamics model for the simulation of the whole human heart. arXiv (2023) <https://doi.org/10.48550/arXiv.2301.02148>
50. Zhong, Z., K. Sun, G. Dan, Q. Luo, A. Farzaneh-Far, M. M. Karaman, and X. J. Zhou. Visualization of human aortic valve dynamics using magnetic resonance imaging with sub-millisecond temporal resolution. *Journal of Magnetic Resonance Imaging*. 54(4):1246–1254, 2021. <https://doi.org/10.1002/jmri.27603>.
51. Wiggers, C. J. Modern Aspects of the Circulation in Health and Disease. *Journal of the American Medical Association*. 81(15):1305–1305, 1923. <https://doi.org/10.1001/jama.1923.02650150059033>.
52. Brath, P. C., and J. Eisenach. Atlas of Cardiovascular Monitoring. *Anesthesiology*. 93(1):312–312, 2000. <https://doi.org/10.1097/0000542-200007000-00068>.
53. Caballero, A., W. Mao, R. McKay, C. Primiano, S. Hashim, and W. Sun. New insights into mitral heart valve prolapse after chordae rupture through fluid-structure interaction computational modeling. *Scientific Reports*. 2018. <https://doi.org/10.1038/s41598-018-35555-5>.
54. Bertoglio, C., A. Caiazzo, Y. Bazilevs, M. Braack, M. Esmaily, V. Gravemeier, A. Marsden, O. Pironneau, I. Vignon-Clementel, and W. Wall. Benchmark problems for numerical treatment of backflow at open boundaries. *International Journal for Numerical Methods in Biomedical Engineering*. 34(2):2918, 2018. <https://doi.org/10.1002/cnm.2918>.
55. Africa, P. *life^x*: A flexible, high performance library for the numerical solution of complex finite element problems. *SoftwareX*. 20:101252, 2022. <https://doi.org/10.1016/j.softx.2022.101252>.
56. Africa, P. C., I. Fumagalli, M. Bucelli, A. Zingaro, M. Fedele, L. Dede, and A. Quarteroni. *lifex-cfd*: An open-source computational fluid dynamics solver for cardiovascular applications. *Computer Physics Communications*. 296:109039, 2023. <https://doi.org/10.1016/j.cpc.2023.109039>.
57. Arndt, D., W. Bangerth, B. Blais, M. Fehling, R. Gassmüller, T. Heister, L. Heltai, U. Köcher, M. Kronbichler, M. Maier, P. Munch, J.-P. Pelteret, S. Proell, K. Simon, B. Turcksin, D. Wells, J. Zhang. The deal.II library, version 9.3. *Journal of Numerical Mathematics* 29(3), 171–186 (2021) <https://doi.org/10.1515/jnma-2021-0081>
58. Quarteroni, A., A. Manzoni, and C. Vergara. The cardiovascular system: mathematical modelling, numerical algorithms and clinical applications. *Acta Numerica*. 26:365–590, 2017. <https://doi.org/10.1017/S0962492917000046>.
59. Tezduyar, T., and S. Sathe. Stabilization parameters in SUPG and PSPG formulations. *Journal of Computational and Applied Mechanics*. 4:71–88, 2003.
60. Pope, S. B. Ten questions concerning the large-eddy simulation of turbulent flows. *New Journal of Physics*. 6(1):35, 2004. <https://doi.org/10.1088/1367-2630/6/1/035>.
61. Sagaut, P., and Y.-T. Lee. Large eddy simulation for incompressible flows: An introduction scientific computation series. *Applied Mechanics Reviews*. 55:115, 2002. <https://doi.org/10.1115/1.1508154>.
62. Markl, M., D. Lee, N. Furiasse, M. Carr, C. Foucar, J. Ng, J. Carr, and J. Goldberger. Left atrial and left atrial appendage 4d blood flow dynamics in atrial fibrillation. *Circulation Cardiovascular Imaging*. 9:004984, 2016. <https://doi.org/10.1161/CIRCIMAGING.116.004984>.
63. Markl, M., D. C. Lee, J. Ng, M. Carr, J. Carr, and J. J. Goldberger. Left atrial 4-dimensional flow magnetic resonance imaging: Stasis and velocity mapping in patients with atrial fibrillation. *Invest Radiol*. 51(3):147–154, 2016.
64. Corti, M., A. Zingaro, L. Dede', and A. M. Quarteroni. Impact of atrial fibrillation on left atrium haemodynamics: A computational fluid dynamics study. *Computers in Biology and Medicine*. 150:106143, 2022. <https://doi.org/10.1016/j.combiomed.2022.106143>.
65. Lu, P. C., H. C. Lai, and J. S. Liu. A reevaluation and discussion on the threshold limit for hemolysis in a turbulent shear flow. *Journal of Biomechanics*. 34(10):1361–1364, 2001. [https://doi.org/10.1016/S0021-9290\(01\)00084-7](https://doi.org/10.1016/S0021-9290(01)00084-7).
66. Noack, T., M. Janietz, P. Lurz, P. Kiefer, F. Sieg, M. Marin-Cuartas, R. Spampinato, C. Besler, K.-P. Rommel, D. Holzhey, F.-W. Mohr, J. Ender, M. A. Borger, and J. Seeburger. Dynamic mitral valve geometry in patients with primary and secondary mitral regurgitation: implications for mitral valve repair†. *European Journal of Cardio-Thoracic Surgery*. 56(5):983–992, 2019. <https://doi.org/10.1093/ejcts/ezz096>.
67. Zajac, J., J. Eriksson, P. Dyverfeldt, A. F. Bolger, T. Ebbers, and C.-J. Carlhäll. Turbulent kinetic energy in normal and myopathic left ventricles. *Journal of Magnetic Resonance Imaging*. 41(4):1021–1029, 2015. <https://doi.org/10.1002/jmri.24633>.
68. Baumgartner, H., J. Hung, J. Bermejo, J. B. Chambers, A. Evangelista, B. P. Griffin, B. Iung, C. M. Otto, P. A. Pellikka, and M. Quiñones. Echocardiographic assessment of valve stenosis: Eae/ase recommendations for clinical practice. *European Journal of Echocardiography*. 10(1):1–25, 2009.
69. Harfi, T. T., J.-h. Seo, H. S. Yasir, N. Welsh, S. A. Mayer, T. P. Abraham, R. T. George, R. Mittal. The e-wave propagation index (epi): A novel echocardiographic parameter for prediction of left ventricular thrombus. derivation from computational fluid dynamic modeling and validation on human subjects. *International Journal of Cardiology* 227, 662–667 (2017) <https://doi.org/10.1016/j.ijcard.2016.10.079>
70. Omran, A. S., A. A. Arifi, and A. A. Mohamed. Echocardiography in mitral stenosis. *J Saudi Heart Assoc*. 23(1):51–58, 2010. <https://doi.org/10.1016/j.jsha.2010.07.007>.
71. Lam, B.-K., D. Cosgrove, S. Bhudia, and A. Gillinov. Hemolysis after mitral valve repair: Mechanisms and treatment. *The Annals of thoracic surgery*. 77:191–5, 2004. [https://doi.org/10.1016/S0003-4975\(03\)01455-3](https://doi.org/10.1016/S0003-4975(03)01455-3).
72. Delahaye, J. P., J. P. Gare, E. Viguier, F. Delahaye, G. De Gevigny, and H. Milon. Natural history of severe mitral regurgitation. *European Heart Journal*. 12:5–9, 1991. https://doi.org/10.1093/eurheartj/12.suppl_B.5.
73. Gaasch, W. H., and T. E. Meyer. Left ventricular response to mitral regurgitation. *Circulation*. 118(22):2298–2303, 2008. <https://doi.org/10.1161/CIRCULATIONAHA.107.755942>.
74. Su, B., R. S. Tan, J. L. Tan, K. W. Q. Guo, J. M. Zhang, S. Leng, X. Zhao, J. C. Allen, and L. Zhong. Cardiac MRI based numerical modeling of left ventricular fluid dynamics with mitral valve incorporated. *Journal of Biomechanics*. 49(7):1199–1205, 2016. <https://doi.org/10.1016/j.jbiomech.2016.03.008>.
75. Bavo, A., A. Pouch, J. Degroote, J. Vierendeels, J. Gorman III., R. Gorman, and P. Segers. Patient-specific CFD simulation of intraventricular haemodynamics based on 3D ultrasound imaging. *Biomedical Engineering Online*. 2016. <https://doi.org/10.1186/s12938-016-0231-9>.
76. Bavo, A., A. Pouch, J. Degroote, J. Vierendeels, J. Gorman III., R. Gorman, and P. Segers. Patient-specific CFD models for intraventricular flow analysis from 3D ultrasound imaging: Comparison of three clinical cases. *Journal of Biomechanics*. 2016. <https://doi.org/10.1016/j.jbiomech.2016.11.039>.

Publisher's Note Springer Nature remains neutral with regard to jurisdictional claims in published maps and institutional affiliations.

Authors and Affiliations

Lorenzo Bennati¹ · Giovanni Puppini² · Vincenzo Giamb Bruno³ · Giovanni Battista Luciani³ · Christian Vergara⁴ 

✉ Christian Vergara
christian.vergara@polimi.it

Lorenzo Bennati
lorenzo.bennati@univr.it

Giovanni Puppini
giovanni.puppini@aovr.it

Vincenzo Giamb Bruno
vincenzi.giamb Bruno@aovr.it

Giovanni Battista Luciani
giovanni.luciani@univr.it

¹ Department of Surgery, Dentistry, Pediatrics, and Obstetrics/
Gynecology, University of Verona, Piazzale Ludovico
Antonio Scuro 10, Verona 37134, Italy

² Department of Radiology, University of Verona, Piazzale
Stefani 1, Verona 37126, Italy

³ Division of Cardiac Surgery, Department of Surgery,
Dentistry, Pediatrics, and Obstetrics/Gynecology, University
of Verona, Piazzale Stefani 1, Verona 37126, Italy

⁴ LaBS, Dipartimento di Chimica, Materiali e Ingegneria
Chimica “Giulio Natta”, Politecnico di Milano, Piazza
Leonardo da Vinci 32, Milan 20133, Italy